A New Family of Wurtzite-Phase Cu_2ZnAS_{4-x} and $CuZn_2AS_4$ (A= Al, Ga, In) Nanocrystals for Solar Energy Conversion Applications

Anima Ghosh,[a,b] Soubantika Palchoudhury,*[a] Rajalingam Thangavel,[b] Ziyou Zhou,[a] Nariman Naghibolashrafi,[a] Karthik Ramasamy,*[c] and Arunava Gupta*[a]

Supporting Information

Materials and Methods

Synthesis of wurtzite Cu_2ZnAS_{4-x} and $CuZn_2AS_4$ (A= Al, Ga, In) nanocrystals (CZAS). Cu_2ZnInS_{4-x} nanocrystals (NCs) were synthesized via a simple one-step thermal decomposition method. Specifically, copper (II) acetylacetonate ($Cu(acac)_2$, 99.99+%, 0.2 mmol), zinc (II) acetylacetonate hydrate ($Zn(acac)_2$, 0.1 mmol), indium (III) acetylacetonate ($In(acac)_3$, 0.1 mmol) precursors were heated to 150 °C in the presence of oleylamine (OLA, 10 mL) as a solvent and ligand under N_2 atmosphere using a Schlenk line setup. A mixture of *n*-dodecanethiol (*n*-DDT, 98%, 1 mL) and *tert*-dodecanethiol (*t*-DDT, 1 mL) was quickly injected into the reaction mixture at 150 °C (heating rate, 16 °C/min) as a sulphur and ligand source. The resulting reaction mixture was subsequently heated at 250 °C for 1 h. The cooled solution was cleaned via multiple washes in hexane/ethanol mixture to obtain the final NC product.

To investigate the robustness and general applicability of this synthesis, the reaction was repeated with gallium (III) acetylacetonate ($Ga(acac)_3$, 99.99+%)) and aluminium (III) acetylacetonate ($Al(acac)_3$, 99.99+%)) precursors separately, instead of $In(acac)_3$. Keeping all other parameters the same, CZGS and CZAlS NCs could be formed by heating the respective reactants to 300 °C for 1 h.

The $CuZn_2AS_4$ NC composition was synthesized using 1:2 molar ratio of $Cu(acac)_2$ and $Zn(acac)_2$, keeping all other conditions the same.

The growth of CZAS NCs was studied as a function of reaction time (*e.g.*, 0.5, 1, and 2 h) using x-ray diffraction (XRD) and transmission electron microscopy (TEM). Further, the influence of ligand on phase and morphology control was investigated using different *n*-DDT: *t*-DDT volume ratios (*e.g.*, 0, 1:3, 1:2, 1:1, 2:1, and 3:1) for the CZAS NCs.

The final NC products were readily dispersible in hexane and used for subsequent characterization.

Phase transformation to stannite. The Cu_2ZnAS_{4-x} NCs could be transformed to pure stannite phase by simple annealing of the powder sample at 400 - 450 °C for 2-2.5 h under N_2 atmosphere in a tube furnace. Phase transition to stannite could also be induced in $CuZn_2AS_4$ NCs through annealing at 500 °C under similar conditions.

Characterization. The size and morphology of CZAS NCs were investigated on a FEI Tecnai F-20 transmission electron microscope (TEM, 200 keV) equipped with high angle annular diffraction (HAADF) imaging and energy dispersive x-ray scattering (EDX). The NCs dispersed in hexane were dropped on 300 mesh Ni grids and dried to prepare the samples for TEM. The average elemental compositions of the NCs were investigated using TEM-EDX. The HRTEM images were analyzed using ImageJ software to calculate the NC sizes and inter-fringe distances. Additionally, the powdered NC samples were analyzed using scanning electron microscope (SEM)-EDX (JEOL 7000) to confirm the composition of this new class of material. A Bruker D8 XRD was used to study the crystal phase of the CZAS NCs. Well-dried powdered samples were used in XRD analysis for obtaining good signal-to-noise ratio. Xrda3.1 software was used to fit the experimental XRD pattern and to calculate the corresponding lattice parameters. The CaRIne Crystallography software was used to confirm simulated XRD pattern of all the NCs. Rietveld refinement was also performed to confirm the experimental XRD pattern. Additionally, the valence state of elements in CZAS NCs and the crystal structure were analyzed with a Kratos Axis 165 X-ray photoelectron spectroscope (XPS). The UV absorbance of the NC solutions in hexane was measured on a Shimadzu UV-vis spectrometer to determine the band gaps of different composition CZAS.

Theoretical Calculations. In addition to experimental investigations, first principle calculations were performed to evaluate and compare the optical properties of the $I-II_2-III-VI_4$ quaternary chalcogenides. These were obtained by carrying out self-consistent calculations using the full-potential linearized augmented plane wave plus local orbital (FP-LAPW+lo) method, as implemented in WIEN2K code.[1] Exchange and correlation effects were treated within the Perdew-Bruke-Ernzerhoff (PBE) form[2,3] of the generalized gradient approximation (GGA) and Tran-Blaha

modified Becke-Johnson (TB-mBJ) potential.[4,5] The charge density was Fourier expanded with Gmax=12. The values of Kmax×Rmax=7.0 and lmax=10 were kept constant throughout the calculations. The calculations were iterated until the total energies were converged below 10^{-5} Ry with respect to Brillouin zone integration. The Zn $(3d^{10} 4s^2)$, Cu $(3p^6 4s^2 3d^9)$, In $(4d^{10} 5s^2 5p^1)$, Ga $(3d^{10} 4s^2 4p^1)$, Al $(3s^2 3p^1)$, and S $(3s^2 3p^4)$ orbitals are treated as valence states. In this method, the crystal unit cell is partitioned into non-overlapping muffin-tin spheres (MT) surrounding each atomic and interstitial regions. Inside the muffin-tin spheres (MT), the electronic wave functions and crystal potential were expanded in spherical harmonics. For interstitial regions, plane wave solutions were considered. The muffin-tin radii for Zn, Cu, In, Ga, Al, and S were chosen to be 2.35, 2.25, 2.15, 2.07, 2.05, and 1.90 a.u., respectively. A 2×2×2 division for k-point sampling was used and the tetrahedral method was employed for the Brillouin zone integrations.[6] A supercell of 64 atoms was generated and optimized from principle wurtzite ZnS structure for performing the wurtzite $CuZn_2AS_4$(A= Al, Ga, In) calculations. The band gap values (E_g) of $CuZn_2AS_4$ (A= Al, Ga, In) were calculated from the Tauc's plot, assuming $\alpha^2 \propto (h\nu - E_g)$, where α is the absorption coefficient and $h\nu$ is the photon energy (h is the Planck's constant and υ is the frequency).

To investigate the chemical composition of CZAS NCs, the samples are analyzed using SEM and TEM-EDX. Fig. S1 shows the representative SEM, HAADF, and EDX analysis for Cu_2ZnInS_{4-x} NCs. On the basis of EDX spectra collected from 15 different NCs and different regions within the same NC, the average elemental composition of the NCs is determined to be Cu_2ZnInS_{4-x} (x=0.5±0.3). This is closely related to the stoichiometric amounts used, and similar results are obtained for the Ga and In based NCs. Using similar EDX experiments, the average chemical composition for the second set of NCs is determined to be $CuZn_2AS_{4±0.1}$, as expected from the stoichiometric amounts.
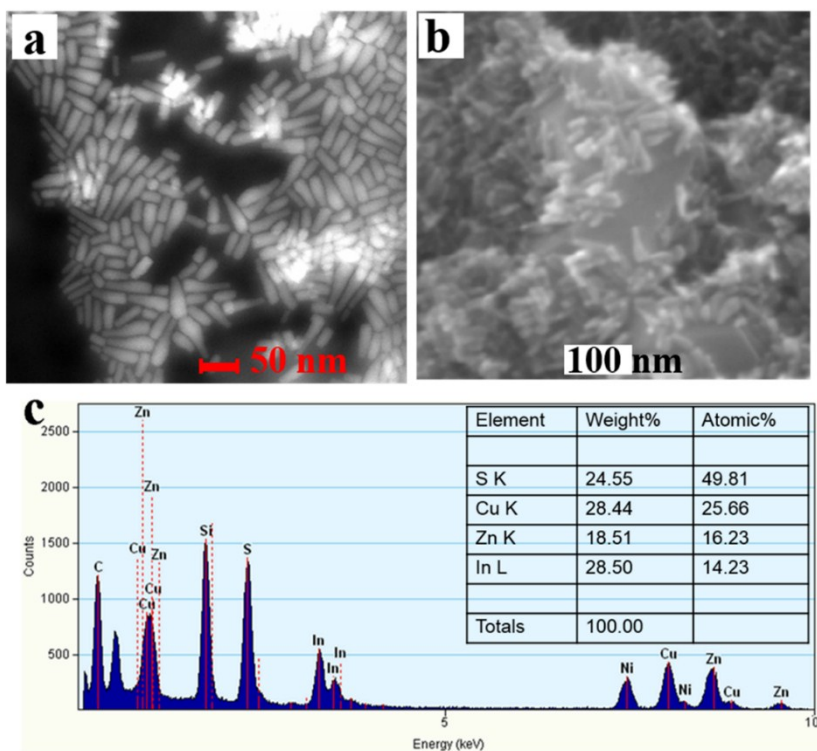

Element	Weight%	Atomic%
S K	24.55	49.81
Cu K	28.44	25.66
Zn K	18.51	16.23
In L	28.50	14.23
Totals	100.00	

Fig. S1 Determination of the average chemical composition of Cu_2ZnAS_{4-x} NCs, representative images shown for A=In. (a) HAADF-STEM image, (b) SEM image, and (c) TEM-EDX plot with inset showing the elemental composition.

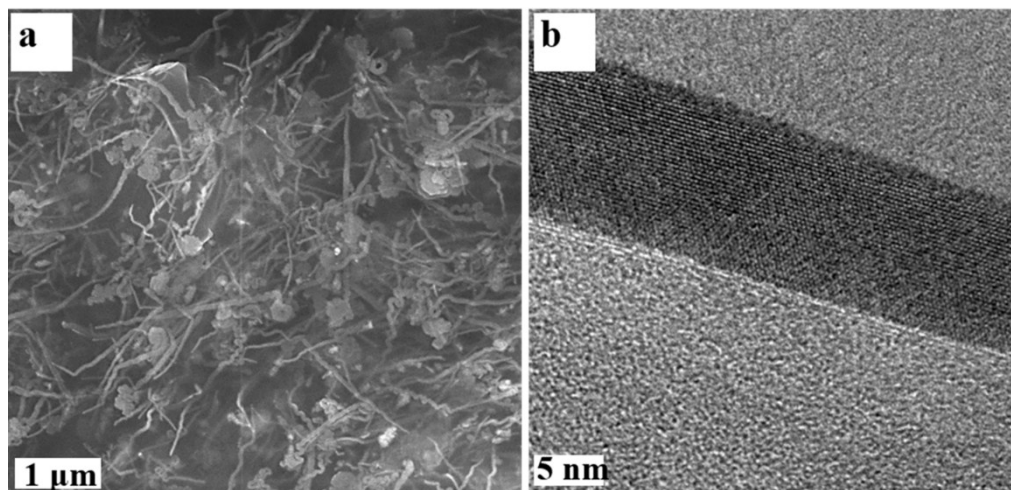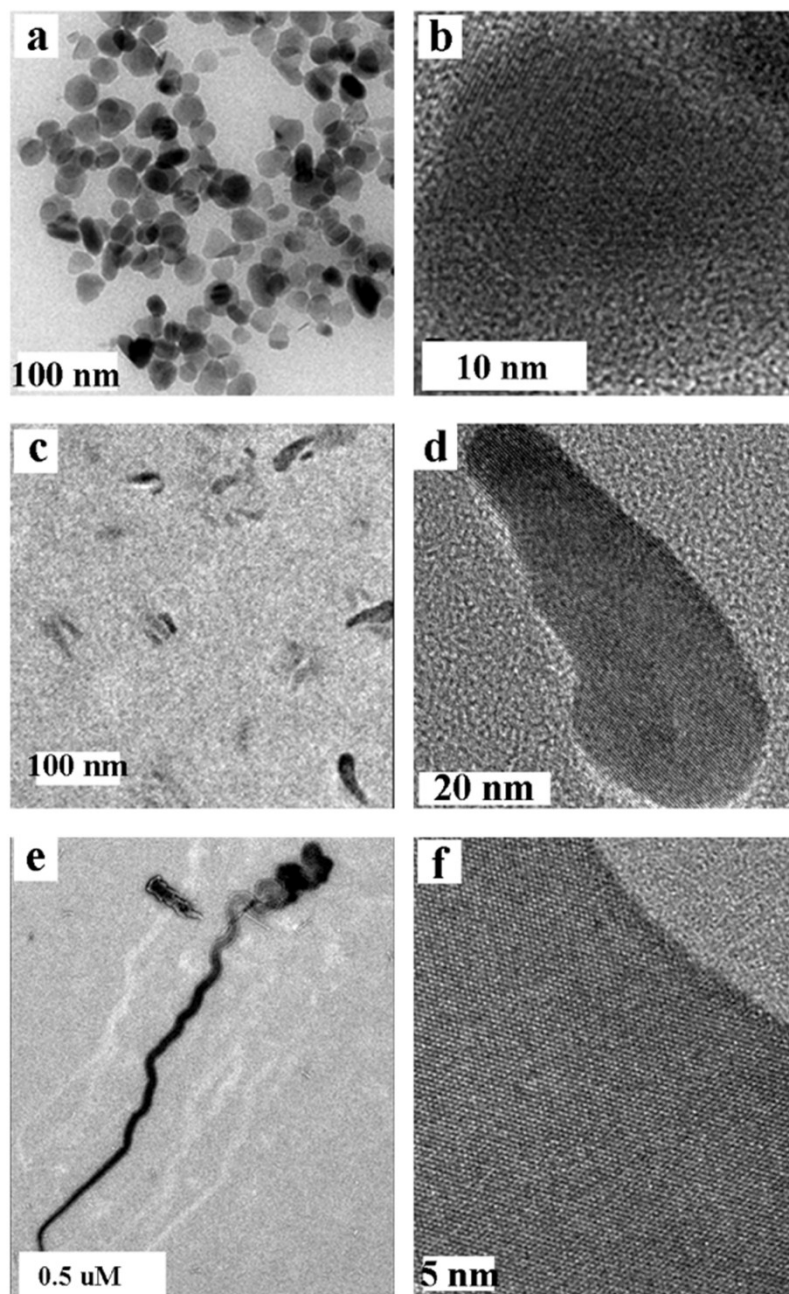**Fig. S2** SEM and HRTEM images of the $CuZn_2InS_{4\pm0.1}$ NCs of unique long worm-like morphology.

Fig. S3 TEM and HRTEM images of CZAS NCs (A= Al, Ga, In). (a-b) spherical Cu_2ZnAlS_{4-x} NCs, (c-d) tadpole-like Cu_2ZnGaS_{4-x} NCs, and (e-f) worm-like $CuZn_2InS_4$ NCs.
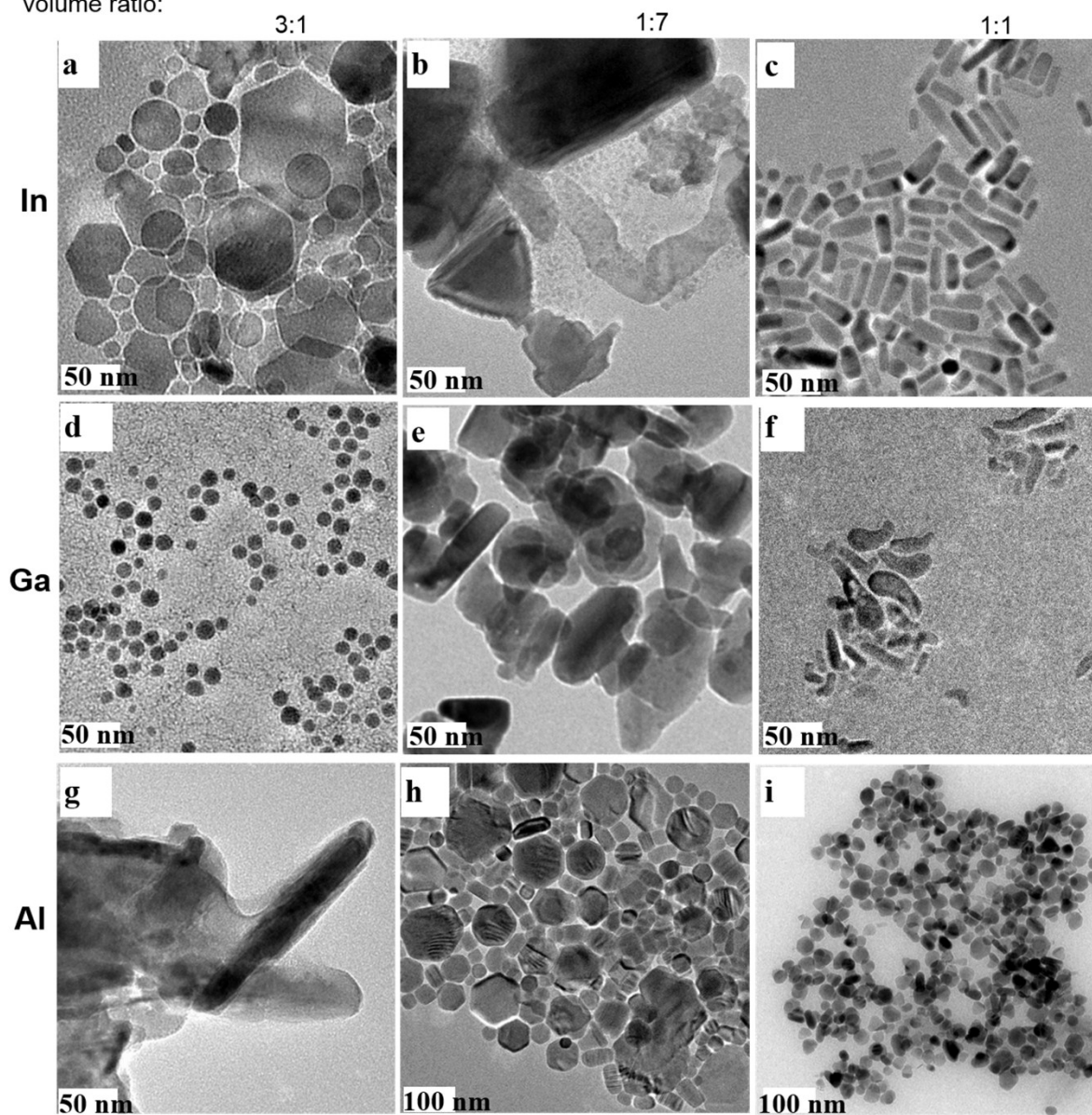
Fig. S4 Critical effect of n-DDT: $tert$-DDT (vol/vol) ligand ratio on Cu_2ZnAS_{4-x} NC formation. (a-c) A= In, (d-f) A= Ga, and (g-i) A= Al.

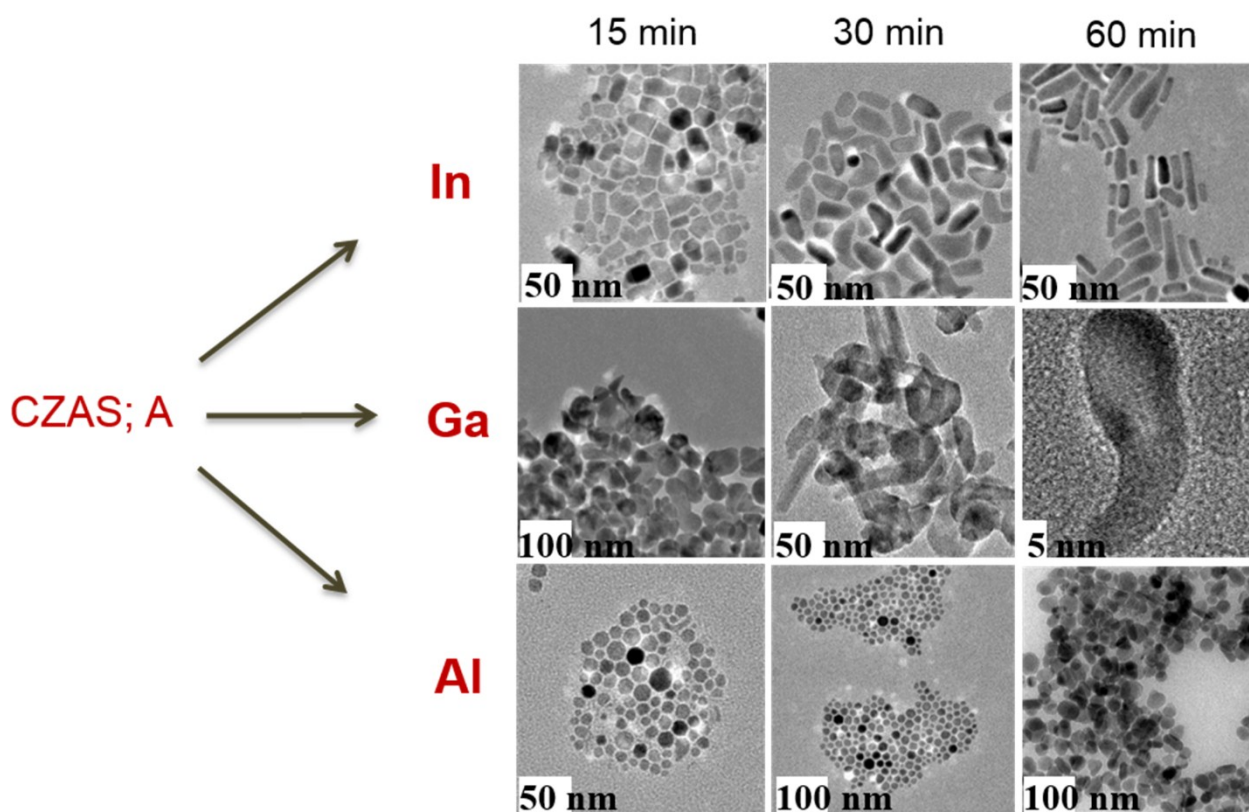**Fig. S5** Schematic diagram showing time-dependent growth morphology of Cu_2ZnAS_{4-x} NCs (A= Al, Ga, In).

To investigate the presence of any binary phase impurities within the CZAS NCs, the XRD plot of the sample are compared with other related binary crystalline phases (Fig. S6). In particular, wurtzite and cubic crystalline phase binary compounds of the related elements (*e.g.*, Ga_2S_3, In_2S_3, Cu_2S, CuS, and ZnS) are plotted, based on the International Centre for Diffraction Data (ICDD) database. The peak positions of these binary phases do not match with the CZAS peaks, indicating their absence in CZAS.
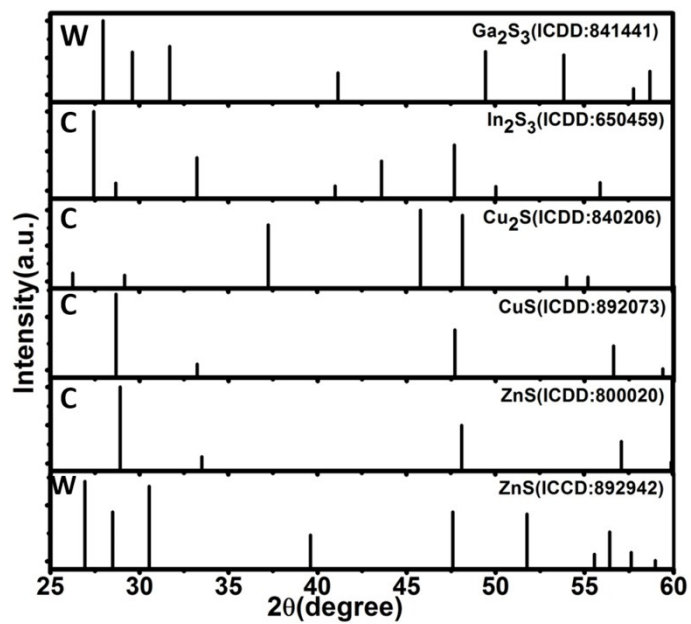
Fig. S6 ICCD XRD patterns for related binary phases; W and C represent the wurtzite and cubic phase, respectively.

Table S1. The structural and optical properties of the new family of wurtzite phase CZAS chalcogenide NCs.

Compound	Lattice parameters		c/a	V (Å^3)	Band gap E_g (eV)	
	a (Å)	c (Å)			Experiment	Theoretical
$CuZn_2AlS_{4\pm0.1}$	3.820	6.305	1.651	79.7	1.72±0.05	1.71
$CuZn_2GaS_{4\pm0.1}$	3.839	6.275	1.634	80.1	1.45±0.04	1.34
$CuZn_2InS_{4\pm0.1}$	3.878	6.394	1.649	83.3	1.42±0.03	1.26
Cu_2ZnAlS_{4-x} (x=0.5±0.3)	3.764	6.198	1.647	76.1	1.60±0.04	
Cu_2ZnGaS_{4-x} (x=0.5±0.3)	3.775	6.239	1.653	76.9	1.50±0.06	
Cu_2ZnInS_{4-x} (x=0.5±0.3)	3.879	6.370	1.642	83.0	1.24±0.07	
Cu_2ZnSnS_4	3.838 [7]	6.338 [7]	1.650 [7]		1.48 [7]	1.18 [8]

The XRD plots for $CuZn_2AS_4$ (A= Al, Ga, In) clearly show a pure wurtzite phase (space group P63mc (No. 186)) with no impurity peaks. Specifically, the peaks match both in position and intensity with the (100), (002), (101), (102), (110), (103), (112), and (201) crystalline planes of wurtzite (Fig. S7a). In addition, these NCs can be readily transformed to the stannite phase (space group $I\bar{4}2m$; no. 121) after annealing (Fig. S7b).
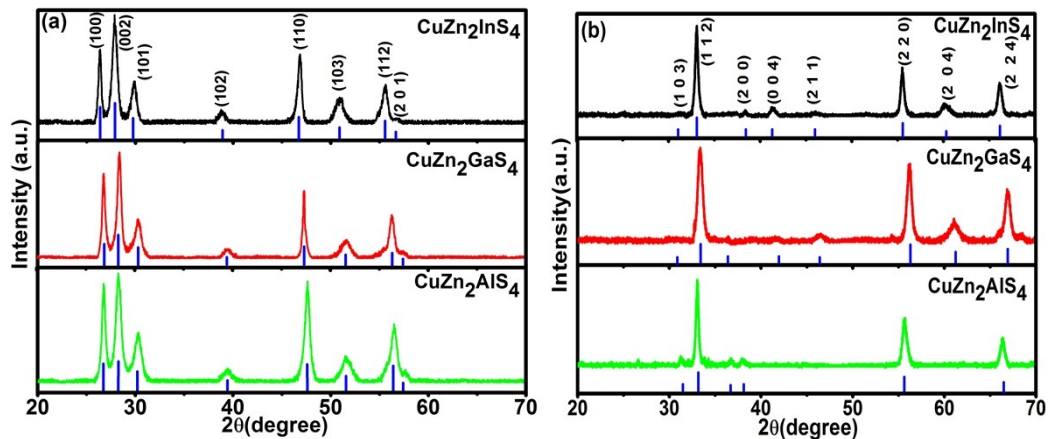

Fig. S7 XRD plots of $CuZn_2AS_{4\pm0.1}$ NCs showing (a) pure wurtzite phase and (b) pure stannite phase after annealing. The blue lines represent simulated pattern for these phases, considering CZAS as cation-disordered phases of ZnS.

Fig. S8 shows the experimental XRD plot, simulated Rietveld fit, difference between the experimental and Rietveld fit, and Bragg reflections for the wurtzite phase $CuZn_2GaS_4$ and stannite phase $CuZn_2InS_4$ NCs. The Rietveld fit for the wurtzite phase CZGS (space group P63mc (No. 186)) is in good agreement with the experimental XRD peaks (Fig. S8a). The experimental data matches well with the stannite structure (space group $I\overline{4}2m$; no. 121), based on the minimum difference and low chi factor (2.3) obtained in the Rietveld refinement (Fig. S8b).
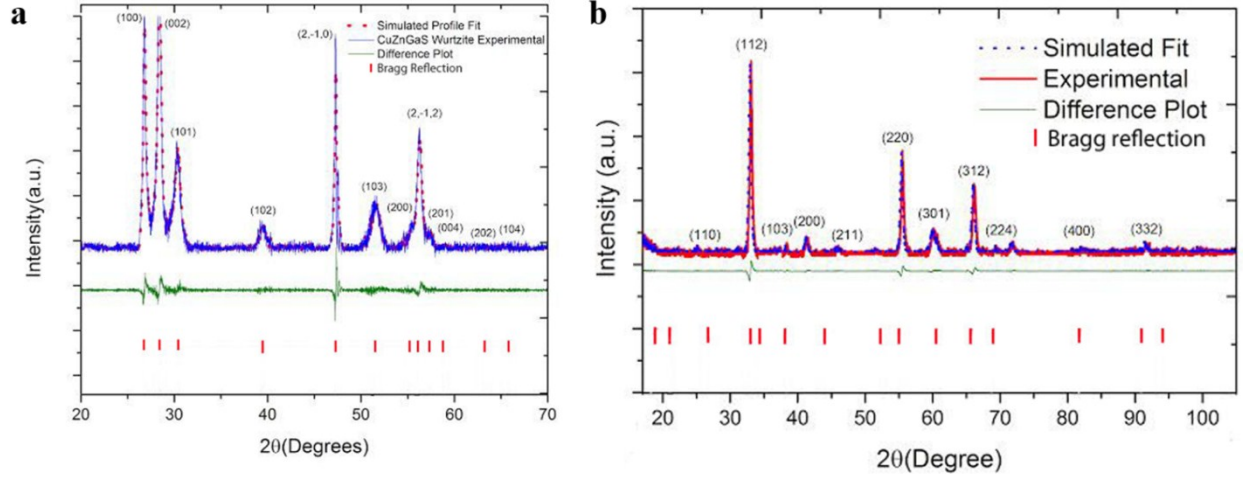

Fig. S8 Rietveld refinement showing good match with the experimental XRD data. (a) Pure wurtzite phase $CuZn_2GaS_{4\pm0.1}$ and (b) pure stannite phase $CuZn_2InS_{4\pm0.1}$ NCs.

Atom	Wyck	*x/a*	*y/b*	*z/c*	Wyck	*x/a*	*y/b*	*z/c*
		Wurtzite				**Stannite**		
S	2b	1/3	2/3	0	8i	0.25374	0.25374	0.12058
Zn	2b	1/3	2/3	0.3752	4d	0	0.5	0.25
In	2b	1/3	2/3	0.3752	2b	0	0	0.5
Cu	2b	1/3	2/3	0.3752	2a	0	0	0

XPS is used to investigate the valence state of the constituent elements in CZAS NCs for confirming the chemical constituents and their valence states. In a representative high-resolution XPS plot of Cu_2ZnInS_{4-x} NCs, the presence of Cu(I), Zn(II), In(III), and S^{2-} oxidation states is inferred based on peak position and splitting (Fig. S9).[9]
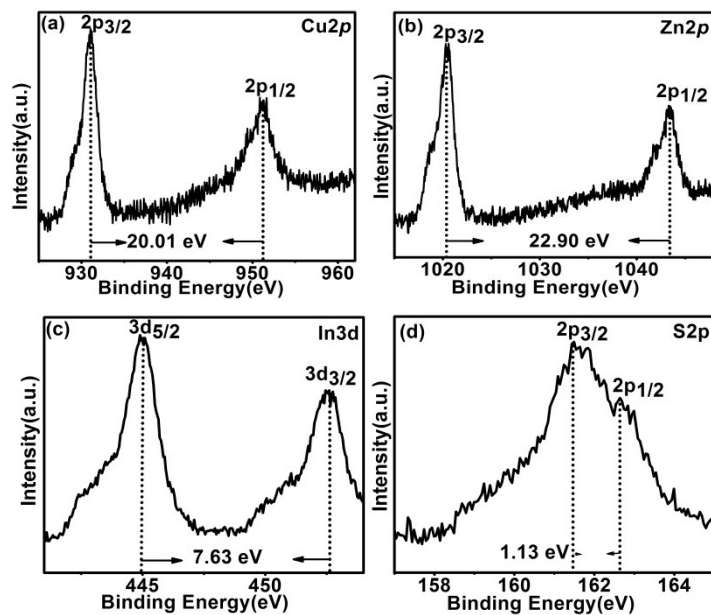

Fig. S9 XPS plots for Cu_2ZnInS_{4-x} (x=0.5±0.3). (a) Cu_{2p} core-level spectra, (b) Zn_{2p} core-level spectra, (c) In_{3d} core-level spectra, and (d) S_{2p} core-level spectra.

Fig. S10 shows the experimental band gap measurements for $CuZn_2AS_{4-x}$ NCs based on UV-vis absorbance.[10] The band gaps are calculated by extrapolating the linear portion of the $(Ahv)^2$ versus photon energy (hv) plots. The band gap values show an increasing trend from In (1.24 eV) to Ga (1.50 eV) and Al (1.60 eV), likely related to decrease in ionic radius. These band gap values are well suited for visible light absorption in solar cells.[11]
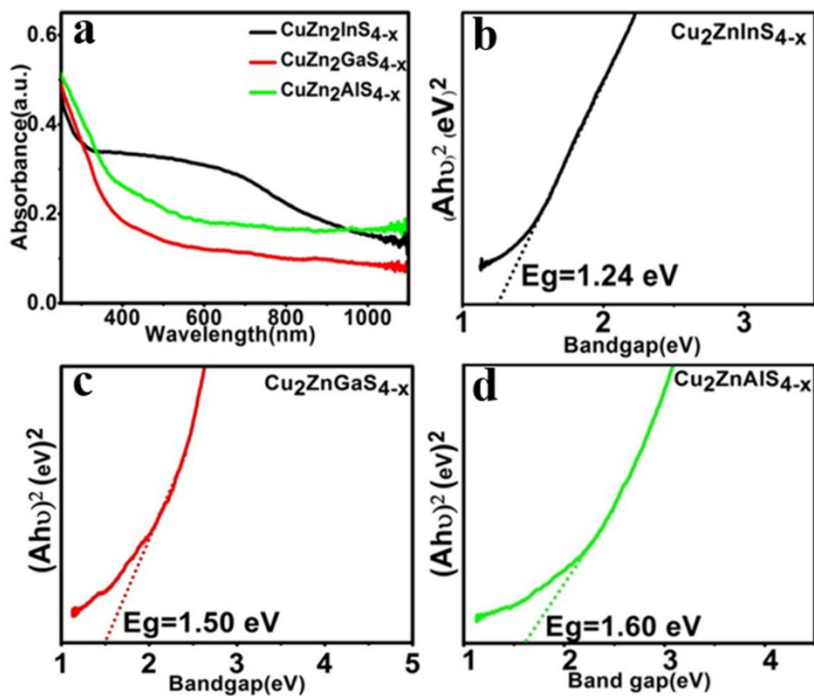

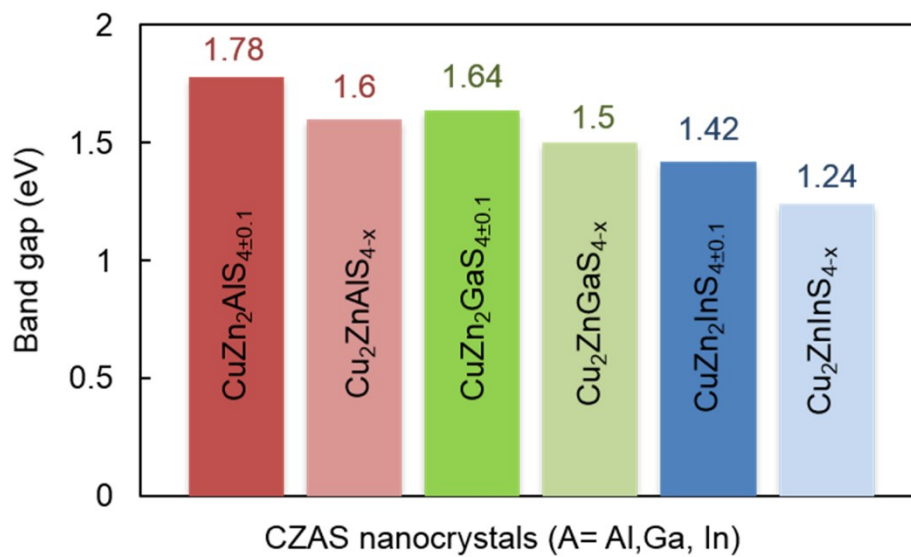**Fig. S10** Band gap measurement of Cu_2ZnAS_{4-x} NCs. (a) UV-vis spectra and (b-d) experimental Tauc plots.

Fig. S11 Illustration of the variable band gap of the synthesized Cu_2ZnAS_{4-x} and $CuZn_2AS_{4\pm0.1}$ NCs (A= Al, Ga, In).

References

1 P. Blaha, K. Schwarz, G.K.H. Madsen, D. Kvasnicka and J. Luitz, WIEN2k, An Augmented Plane Wave Plus Local Orbitals Program for Calculating Crystal Properties (Karlheinz Schwarz, Techn. University at Wien, Austria, 2001).

2 J.P. Perdew, K. Burke and M. Ernzerhof, *Phys. Rev. Lett.*, 1996, **77**, 3865.

3 D. Koller, F. Tran and P. Blaha, *Phys. Rev. B.*, 2012, **85**, 155109.

4 F. Tran and P. Blaha, *Phys. Rev. Lett.*, 2009, **102**, 226401.

5 C. Shiyou, X.G. Gong, W. Aron and S.H. Wei, *Appl. Phys. Lett.*, 2009, **94**, 041903.

6 H.J. Monkhorst and J.D. Pack, *Phys. Rev. B.*, 1976, **13**, 5188.

7 K. Ramasamy, X. Zhang, R. D. Bennett and A. Gupta, *RSC Adv.*, 2013, **3**, 1186.

8 A. Ghosh, R. Thangavel and M. Rajagopalan, *Mater. Sci.*, 2013, **48**, 8259.

9 H. Virieux, M. Le Troedec, A. Cros-Gagneux, W.-S. Ojo, F. Delpech, C. Nayral, H. Martinez and B. Chaudret, *J. Am. Chem. Soc.*, 2012, **134**, 19701.

10 C. Jiang, J.-S. Lee, D.V. Talapin, *J. Am. Chem. Soc.*, 2012, **134**, 5010.

11 A.J. Wooten, D.J. Werder, D.J. Williams, J.L. Casson and J.A. Hollingsworth, *J. Am. Chem. Soc.*, 2009, **131**, 16177.